Available online at www.sciencedirect.com
SCIENCE DIRECT®
International Journal of Heat and Mass Transfer 47 (2004) 1129–1140
International Journal of HEAT and MASS TRANSFER
www.elsevier.com/locate/ijhmt

Fluid-flow and endwall heat-transfer characteristics of an ultralight lattice-frame material

T. Kim, H.P. Hodson, T.J. Lu *

Department of Engineering, University of Cambridge, Trumpington Street, Cambridge, CB2 1PZ, UK

Received 19 October 2002; received in revised form 10 October 2003

Abstract

This paper describes an experimental study of the pressure loss and endwall heat transfer in a highly porous, ultralightweight, multifunctional lattice-frame material (LFM) subjected to forced air convection. The influence of LFM morphology on the endwall flow and heat transfer patterns in a unit cell is examined in detail. Depending on the orientation of the LFM, the pressure loss across a unit cell was found to be between about 30% and 60% of the dynamic pressure over a wide range of Reynolds numbers. For the two selected orientations, the LFM has almost the same overall heat transfer performance.

Detailed endwall surface heat transfer distributions were obtained using thermochromic liquid crystals (TLCs). The results reveal that the local endwall heat transfer was sensitive to details such as the location of vertices and the inclination angle of struts. High heat transfer regions were clearly observed around the vertices due to the formation of horseshoe vortices and behind the inclined and/or yawed struts. It was also found that the use of high conductivity materials such as aluminum alloy for the struts enhances the rate of heat transfer by a factor of approximately 2.5 when compared to using a low conductivity material such as polycarbonate.

1. Introduction

A variety of technologies such as pin fins, cylinder banks and wire screens have been developed in the past century to increase the heat transfer area density of a heat sink without increasing its overall dimensions. More recently, cellular metallic foams have been used to construct lightweight and compact heat sinks. The high thermal conductivity of metal, combined with the ability of the foam to promote eddies and mix the coolant fluid, has enabled such heat sinks to remove up to five times more heat than that by a traditional pin-fin array, at a third of the weight, although the increase in the pressure drop is relatively high [1–5].

With an ever increasing demand for higher power heat exchangers, a broad range of novel heat exchanger media has been reported. However, in terms of carrying both mechanical and thermal loads, little work on multifunctional heat exchangers exists. In situations where a heat sink is also carrying a large structural load (e.g. the jet blast deflector on an aircraft carrier), a lattice-frame material (LFM) appears to be more attractive than conventional heat dissipation media. The LFM is a new development made possible by computer-based design and numerically controlled processing. It consists of a three-dimensional (3D) network of cylindrical struts (Fig. 1). The stretching-dominated LFM structure is about 10 times stiffer and 3 times stronger than the bending governed metal foams at the same porosity level (~0.9) [6,7]; and these ratios increase with increasing porosity. Details of the mechanical properties of the LFM can be found in [7,8].

For the LFM studied in this paper, the diameter of the strut is on the order of one millimeter and the relative density of the product is approximately 6%. (The relative density is defined as the ratio of the LFM structure density to the density of the solid of which it is

* Corresponding author. Tel.: +44-1223-766316; fax: +44-1223-332662.
E-mail address: tjl21@cam.ac.uk (T.J. Lu).

0017-9310/$ - see front matter © 2003 Elsevier Ltd. All rights reserved.
doi:10.1016/j.ijheatmasstransfer.2003.10.012

Nomenclature

d	LFM strut diameter [m]
d_p	unit cell length of the LFM [m]
h	heat transfer coefficient [W/m^{2}K]
H, L, W	height, length and width of test sample [m]
K_{Cell}	pressure loss coefficient ($\Delta P_{Cell}/\rho U^2/2$)
k_s, k_f	thermal conductivity of solid and fluid [W/m K]
l	LFM strut length [m]
LFM	lattice-frame material
LM25, P	aluminum alloy and polycarbonate LFM samples
Nu_{dp}	Nusselt number based on unit cell length (hd_p/k_f)
O-A, O-B	orientation A and orientation B of the LFM
ΔP	static pressure loss [Pa]
ΔP_{Cell}	static pressure loss per unit cell length ($\Delta P \cdot d_p/L$) [Pa]
Re_{dp}	Reynolds number based on unit cell length ($\rho U d_p/\mu$)
t	time [second]
T	temperature [K]
TLCs	thermochromic liquid crystals
x, y, z	coordinate system; x (mainstream direction), y (channel width), z (channel height)

Greek symbols

ε	porosity
μ	viscosity of coolant (air) [kg/(s m)]
ρ	density of coolant [kg/m^3]

Subscripts

average	spatially averaged value over unit cell
dp	the LFM unit cell based value
final	final steady-state value
init	initial value (at $t = 0$)
S	solid surface

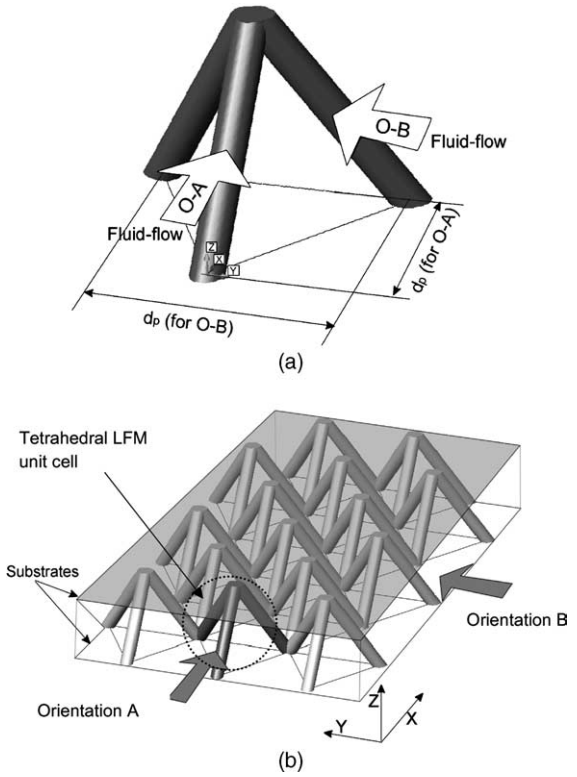

Fig. 1. LFM configuration: (a) one tetrahedral unit cell and (b) a block of unit cells.

made.) The overall pressure drop and averaged heat transfer measurements on the LFM were reported in [9]. However, details of the fluid-flow and heat-transfer patterns in the LFM heat sink were not studied in [9] due to experimental limitations. In this paper, the investigation of heat-transfer and fluid-flow characteristics of the LFM focuses on the pressure drop per unit cell and the detailed effects that the lattice structure has on local heat transfer distributions and flow patterns. In addition, the measurements obtained using the transient liquid crystal thermography will be compared with those obtained from the steady-state experiments in [9]. The results will be used in a separate study to validate computational fluid dynamics (CFD) simulations and analytical models. The ultimate goal is to establish a comprehensive optimization methodology for designing weight efficient, multi-functional compact heat exchangers.

2. Experimental details

2.1. Experimental apparatus

The endwall surface heat-transfer characteristics of the LFM heat exchanger were examined by employing the transient liquid crystal thermography technique. Details of the experimental apparatus and the LFM samples used for the transient measurements are presented below.

Fig. 2(a) shows the testing rig developed in [9] for the steady-state experiments, whereas Fig. 2(b) shows its modified version for the present transient tests. In general, the experimental apparatus consists of four main

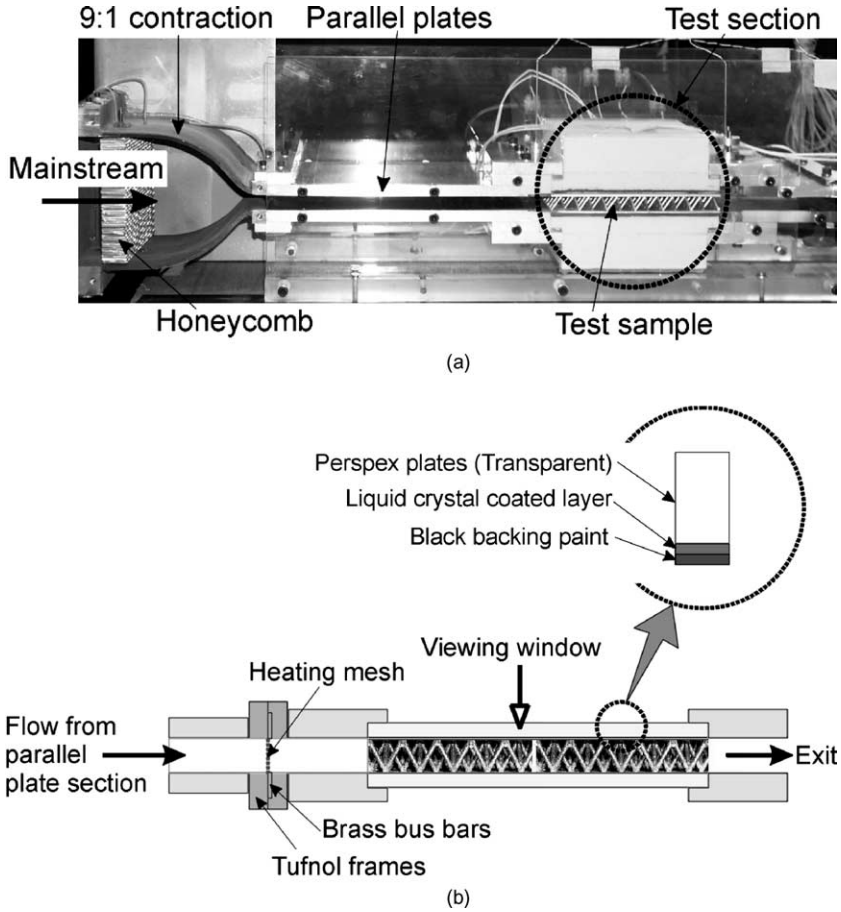

Fig. 2. Forced air convection test rig for: (a) steady-state experiments and (b) transient measurements with liquid crystal thermography.

items: the coolant supply, the test section including the heating mesh at the inlet, the test sample, and the data acquisition system. Air at ambient conditions is drawn through the channel passage by a suction device. The coolant enters through a 9:1 contraction followed by a parallel section before it reaches the test section; the ratio of section length to channel height is 20.

2.2. LFM samples for steady-state experiments

Fig. 1 shows the two different flow orientations used in the present test. Two aluminum alloy sandwich panels (for orientation A and B) and one polycarbonate sandwich panel (for orientation A) were fabricated and tested (Table 1) for the steady-state experiments. The endwalls and LFM struts of the former models were made of LM25 Al casting alloy. For the latter, its LFM core was made from polycarbonate but the endwalls were made of 1 mm thick pure aluminum plate. Due to the very low thermal conductivity of the polycarbonate (approximately 0.2 W/m K), it is reasonable to assume that there is no heat transfer carried out from the LFM strut surface. Another polycarbonate sample was also used for the transient heat transfer experiments using thermochromic liquid crystals (TLCs). This model has the polycarbonate LFM core and 6 mm thick Perspex endwalls.

The dimensions of the test samples are 0.127 m (width), 0.012 m (height) and 0.127 m (length). The diameter of the LFM struts is 2 mm. The ratio of strut length to diameter is 7.35, and the relative density of the test samples is approximately 6%, namely the porosity is 0.94. A total of four static pressure tappings were placed on the upper endwall along the flow direction. All four samples were used for the pressure drop measurements.

2.3. Transient endwall heat transfer using thermochromic liquid crystals

To obtain thermal maps on the endwalls, TLCs were sprayed on the surface to monitor the evolution of surface temperature with time. The temperature sensitive

Table 1
Morphology parameters of LFM samples

Samples	LM25 (O-A)	LM25 (O-B)	P (O-A)
Relative density (ρ)		0.062	
Porosity (ε)		0.938	
Surface area density		123.68 m^{-1}	
LFM strut diameter (d)		0.002 m	
LFM strut length (l)		0.0147 m	
Longitudinal cell pitch		0.0127 m	
Transverse cell pitch		0.0147 m	
Cell height (H)		0.012 m	
Material	LM25 Al alloy	LM25 Al alloy	Polycarbonate core with pure Al endwalls
Solid thermal conductivity (k_s) [W/m K] at 20 °C	150.86	150.86	0.19–0.22

liquid crystals selectively display colours with respect to temperature. When a solid plate is exposed to a sudden step increase of fluid temperature, a thermal pulse penetrates the solid plate. This is a classical transient one-dimensional (1D) semi-infinite plate problem with a step change of fluid temperature boundary condition. However, because of the finite thickness of the solid plate, the solution is limited by the time needed for the thermal pulse to traverse the plate thickness.

In order to provide a sudden change in air temperature, a heating mesh was used [10,11]. The wire heating mesh (made of 36 μm diameter stainless steel wires) was sandwiched between two Túfnol frames after being soldered to brass bus bars. The bus bars are used to connect the heating mesh to a low voltage and high current transformer. While air is passing through the heating mesh, the heat generated by the electrical current is transferred to the air. A schematic diagram of the transient test section that was modified to fit into the steady-state experimental rig (Fig. 2(a)) is shown in Fig. 2(b). The polycarbonate single layered LFM was sandwiched between two 6 mm thick Perspex plates. Before an upper plate (used as a viewing window) was attached to the top of the LFM, the TLCs (BM/R27C6W/C17-10) and then black backing paint (BB-G1) from Hallcrest Inc. were sprayed onto the inner airside surface of the plate.

During the transient experiments, the colour changes of the TLCs on the endwall (i.e., the inner plate surface) were monitored using a digital camera (SONY DCR-PC110E). The TLC images in the Red, Green and Blue (RGB) space were then converted into the Hue, Saturation and Intensity (HSI) space using the IMAQ™ software which is part of LabVIEW™. After conversion into HSI space, the hue values of the images were converted into temperatures using a previously determined calibration. The evolution of temperature at each pixel in the captured thermal images was then used to determine the heat transfer coefficient at that location. Details of the data reduction are described in the next section.

3. Data reduction

3.1. Determination of unit cell length

Since the LFM is structurally anisotropic, it is necessary to determine a characteristic length, d_p, corresponding to the orientation of the structure relative to fluid flow. Two orientations such as orientation A and B (O-A and O-B as shown in Fig. 1) were selected for the investigation. Different length scales are expected although both orientations have the same porosity of 0.94. The characteristic length is chosen as the pitch of the tetrahedral LFM unit cells (Fig. 1) in the flow direction. Thus, $d_p = l\cos(\pi/6) = 0.0127$ m for orientation A and $d_p = l = 0.0147$ m for orientation B, where l is the LFM strut length.

3.2. Pressure loss coefficient, K_{Cell}

The pressure loss across the LFM structure occurs mainly as a result of form drag rather than viscous drag. Also the flow patterns repeat every cell. Therefore, rather than the traditional friction factor, the pressure loss coefficient per unit cell, K_{Cell}, is used to present the data:

$$K_{Cell} = \frac{\Delta P_{Cell}}{\rho U^2/2} \tag{1}$$

where ΔP_{Cell} is the static pressure loss per unit cell and $\rho U^2/2$ is the dynamic pressure based on the mean inlet velocity, U. Similarly, the Reynolds number based on the unit cell length is defined as:

$$Re_{d_p} = \frac{\rho U d_p}{\mu} \tag{2}$$

where ρ and μ are the density and viscosity of air.

3.3. Heat transfer coefficient and Nusselt number

It is common practice in transient heat transfer experiments to assume that there is a step change in the

thermal boundary condition. The analytical 1D solution for a semi-infinite plate exposed to such a step is then used to find the heat transfer coefficient from the measured surface temperature history. However, in the present experiments, the air temperature increases exponentially with time as

$$\Theta_f(t) = \frac{T_f(t) - T_{init}}{T_{final} - T_{init}} = 1 - e^{-t/\tau} \quad (3)$$

where the time constant τ is of the order of 0.1 s. The actual value depends on the thermal capacity of the heating mesh and its heat transfer coefficient. In this case, the 1D solution for the plate surface temperature $T_s(t)$ associated with a step increase of fluid temperature could be replaced by either the sum of the solutions for a series of step changes or a solution for an exponential increase in fluid temperature [10,11]. A modified 1D solution based on the exponential increase of fluid temperature developed in [10] will be used here

$$\Theta_s(t,\tau) = \frac{T_S(t) - T_{init}}{T_{final} - T_{init}} = f(\beta, \beta_\tau) \quad (4)$$

where $T_s(t)$ is the surface temperature measured by the liquid crystal, T_{final} is the final steady-state fluid temperature, T_{init} is the initial solid and fluid temperature, and

$$f(\beta,\beta_\tau) = 1 - \frac{1}{1+\beta_\tau^2} e^{\beta^2} \operatorname{erfc}(\beta) - e^{-t/\tau} \frac{\beta_\tau^2}{1+\beta_\tau^2} \times \left\{ 1 + \frac{1}{\beta_\tau} \left[\frac{1}{\pi} \sqrt{\frac{t}{\tau}} + \frac{2}{\pi} \sum_{n=1}^{\infty} \frac{1}{n} e^{-n^2/4} \sinh\left(n \sqrt{\frac{t}{\tau}} \right) \right] \right\}$$

Here, $\beta = h\sqrt{\alpha t}/k$, $\beta_\tau = h\sqrt{\alpha\tau}/k_s$, h is the surface heat transfer coefficient, τ is the time constant to be measured, α is the thermal diffusivity of the plate material, and erfc is the complementary Gaussian error function.

With the measured surface temperature change in time for a given location, the local heat transfer coefficient h can be calculated implicitly from Eq. (4). In Fig. 3, for example, a comparison is made between the measured and estimated values of $T_s(t)$ based on an ideal single step or a single exponential increase. The quality of the comparison is associated with the choice of the thermal boundary condition (e.g., step increase or single exponential increase of the fluid temperature) in the determination of the surface heat transfer coefficient. In the example case shown in Fig. 3, the error in the heat transfer coefficient due to the assumption of a step increase is approximately 3%. In general, the modified equation (4) follows the experimental data well (Fig. 3).

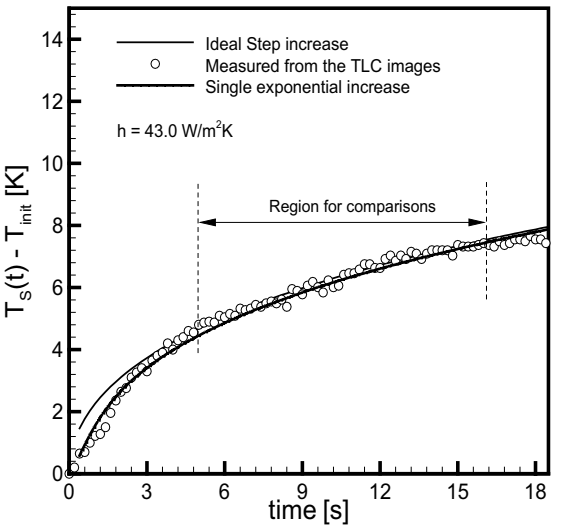

Fig. 3. Typical temperature history from TLC images compared with that predicted by 1D semi-infinite solid plate solution.

The local Nusselt number based on unit cell length is defined as

$$Nu_{d_p} = \frac{h}{k_f/d_p} \quad (5)$$

where h is the heat transfer coefficient obtained implicitly from Eq. (4), and k_f is the thermal conductivity of air.

3.4. Measurement uncertainties

An uncertainty analysis mainly for random errors was performed using the method of Coleman and Steele [10]. It was assumed, for the transient measurements, that systematic errors could be minimized by careful calibrations. For the pressure drop measurements, the static pressure change as a result of air density change due to temperature variations was small, since the operating temperature range is small (typically less than 20 K). The uncertainty associated with the static

Table 2
Estimated experimental uncertainties for transient measurements

Measurement	Typical value	Standard error	Estimated error%
Transient test time (t)	20 s	0.1 s	0.5
Product ($\sqrt{\rho c_p k}$)	559 W s$^{1/2}$/m^2 K	14 W s$^{1/2}$ /m^2 K	2.5
$\Delta T_f(T_{final} - T_{init})$	20 K	0.2 K	1.0
$\Delta T_S(T_S - T_{init})$	7 K	0.4 K	5.7

pressure loss and the corresponding pressure loss coefficient was estimated to be less than 0.1% and 1.7%, respectively.

The estimated uncertainties associated with the use of the TLCs are presented in Table 2 where T_f, T_s and T_{init} are the fluid temperature, solid surface (coated with a thin liquid crystal layer) temperature and initial temperature, respectively. The total uncertainties of the local heat transfer coefficient and of the Nusselt number were estimated to be 6.3% and 9.1%, respectively.

4. Results and discussion

4.1. Pressure loss coefficient (pressure drop per unit cell)

The pressure losses associated with the LFM are expressed in terms of a new parameter, namely, the static pressure loss per unit cell, K_{Cell}. Observations on open-celled metal foams [13] show that the fluid-flow patterns repeat in each unit cell, excluding the cells near the entry and exit regions. In fact, the entry and exit regions in both metal foams and the LFM are short, with a typical length of about one or two unit cells (see [13] and the results presented below). Thus, information concerning a representative unit cell can be utilized to express the overall hydraulic behaviour of the highly porous structures. When designing a heat exchanger, for example, it is important to know the overall pressure loss, which can be calculated by simply multiplying K_{Cell} with the total number of unit cells in the flow direction.

The results of the pressure loss measurements in the LFM are depicted in Fig. 4. These indicate that the fluid-flow is typically in the laminar regime when $Re_{dp} < 2000$. Here, viscous effect dominates as:

$$K_{Cell} = C(Re_{dp})^{-1}$$

where C was found to be about 1000 for orientation A. In comparison, C is 64 for laminar pipe flow when using the hydraulic channel diameter as the length scale. Flow transition from laminar to turbulent occurs when $2000 < Re_{dp} < 3000$. It is clearly seen in Fig. 4 that the transition of the polycarbonate model occurs later due to the smoother surface compared to that of the LM25 model. The pressure loss coefficients of all three samples approach asymptotic values after the flow transition. This is because form-dominated flow prevails at Reynolds numbers larger than 3000. Here, pressure drag is dominant, with K_{Cell} = constant.

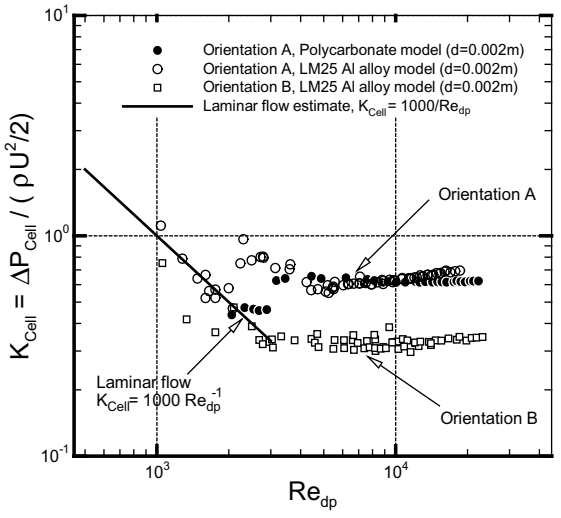

Fig. 4. Pressure loss coefficient (pressure drop per unit cell length) plotted as a function of Reynolds number.

Because of the structural anisotropy of the LFM, the pressure drop varies depending on the sample orientation with respect to the fluid-flow. The results for both the orientations reveal that, in the high Reynolds number regime ($Re_{dp} > 3000$), the pressure loss per unit cell is approximately 60% and 30% of the dynamic pressure for orientation A and orientation B, respectively. The overall pressure loss of orientation A from both the LM25 and polycarbonate models has the same asymptotic value at high Reynolds numbers. This is due to the predominance of form drag at high Reynolds numbers.

The flow resistance encountered by the flow in orientation A is twice as large as that in orientation B, because the staggered array like-configuration of struts in orientation A causes a higher flow blockage and consequently higher internal velocities although the same wetted surface as that in orientation B is maintained. It will be shown later that orientation B and orientation A have almost the same heat transfer performance. Therefore, orientation B is preferable when pumping power is an issue.

4.2. Endwall fluid-flow and heat-transfer characteristics

4.2.1. Anisotropy of the LFM

The fluid-flow and heat-transfer characteristics in the LFM are very complicated because of the 3D flow field within the structure. To describe the structural anisotropy of the LFM that leads to the aerodynamic anisotropy, flow in the x–y plane parallel to the endwalls of both orientation A and B are schematically illustrated in Fig. 5. Orientation A is a configuration that provides the most closed flow passage and orientation B is an orientation that is rotated 90° with respect to the mainstream as illustrated in Fig. 1(a,b). The latter provides the most open flow passage.

At a given cell height position (i.e., z = constant), the LFM unit cell is formed by an equilateral triangle with

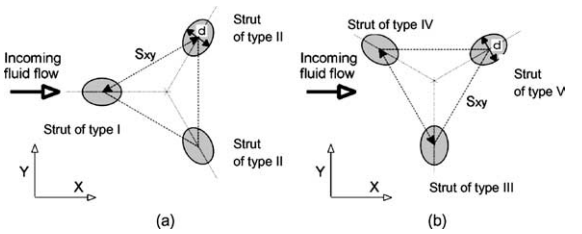

Fig. 5. Flow in x–y plane for: (a) orientation A and (b) orientation B.

cylindrical struts of elliptical cross-sections. Due to the unique LFM morphology, the ratio of the distance between two cylinders S_{xy} to the cylinder diameter d, varies with the location along the z-axis. For instance, at $z = 0$ (bottom endwall), the spacing ratio $S_{xy}/d = 7.35$ and, at $z = H$, $S_{xy}/d = 0$. With respect to Fig. 5(a), the fluid-flow for orientation A is expected to be symmetric about a line of constant 'y' value through the centre of each vertex of the LFM. For orientation B (see Fig. 5b), the flow pattern is asymmetrical with respect to the incoming mainstream. The above discussion suggests that two completely different thermal-flow patterns may exist on the endwall.

To investigate the effect of the anisotropy of the LFM on endwall surface flow pattern and the corresponding overall heat transfer performance, endwall surface heat transfer distributions were measured by using the TLC technique with the polycarbonate LFM models consisting of polycarbonate LFM core sandwiched between Perspex endwalls. After the image processing, the detailed heat transfer distribution on endwall surfaces was obtained. The use of polycarbonate with low thermal conductivity (~0.2 W/m K), in comparison with the highly conducting aluminum alloy, minimized the conduction of heat through LFM struts and in the endwalls.

4.2.2. Orientation A

Fig. 6(a) presents the experimentally obtained Nusselt number distribution on the lower endwall where the Reynolds number Re_{dp} is 4600. A short entry region is present, being no more than one unit cell in length. A similar endwall heat transfer pattern is repeated at each vertex beyond the first cell of each row. The endwall heat transfer patterns at each vertex are symmetric with respect to the centre of the vertex and the flow direction (x-axis). High heat transfer regions in front of and a short distance behind the vertices are observed. The former is due to the formation of a horseshoe-type vortex, whereas the latter results from the flow recirculation and flow reattachment of the wakes of the inclined and yawed struts. Fig. 6(b) displays the detail of two adjacent unit cells, highlighting the two aforementioned high heat transfer regions.

4.2.3. Orientation B

Fig. 7(a) presents the measured endwall Nusselt number distribution of orientation B at $Re_{dp} = 6000$. The effect of the entry on the endwall surface heat transfer distribution appears to persist through most of the test model length although the effect diminishes rapidly after the first few cells. In general, two distinct endwall flow features were observed. One is due to the serpentine-shaped flow passage. The flow near the endwall surface associated with this flow pattern experiences less interference from the presence of the struts and vertices. This results in a lower heat transfer than elsewhere. The second feature is a region of high heat transfer, which occurs near the vertices where there is a strong flow interaction.

A single unit cell was selected from a central location and is depicted in Fig. 7(b). As can be seen from Fig. 1, three different types of struts form the unit cell in the orientation B. Fig. 7(b) shows that the wake behind each vertex are skewed and asymmetric as a result of the asymmetric arrangement of the struts. In addition, the location of the centre of the flow passage on the endwall surface appears to coincide with where a vertex is situated on another endwall plate. At this location, the least flow blockage is present.

The high heat transfer occurs in front of and behind the vertex as is the case in orientation A. However, in contrast to orientation A, the horseshoe vortex is now skewed. The wakes from the connected struts cause the aforementioned high heat transfer region behind the vertex.

4.3. Effect of entry and exit regions on the overall heat transfer

In order to examine the local variation of the endwall surface heat transfer along the flow direction, the measured local Nusselt number was spatially averaged for each unit cell from the entry region to the exit region. Fig. 8 presents the variation of the cell-averaged endwall Nusselt number normalized by the averaged Nusselt number from third to seventh cell. The latter values represent the fully developed flow patterns. It should be noted that none of these values include a contribution from the struts.

The first cell of orientation A has a Nusselt number which is about 65% of the average Nusselt number, whilst that of orientation B has a value which is 85% of the average Nusselt number. This indicates that orientation B suffers less from entry effects than orientation A in terms of the overall endwall heat transfer. In fact, for orientation A the effect of the entry region is to decrease the overall heat transfer about 6% when 8 unit cells are used in the flow direction. For orientation B, the entry region causes a decrease of 2.5% of the overall heat transfer when 7 unit cells was used. The model length, L,

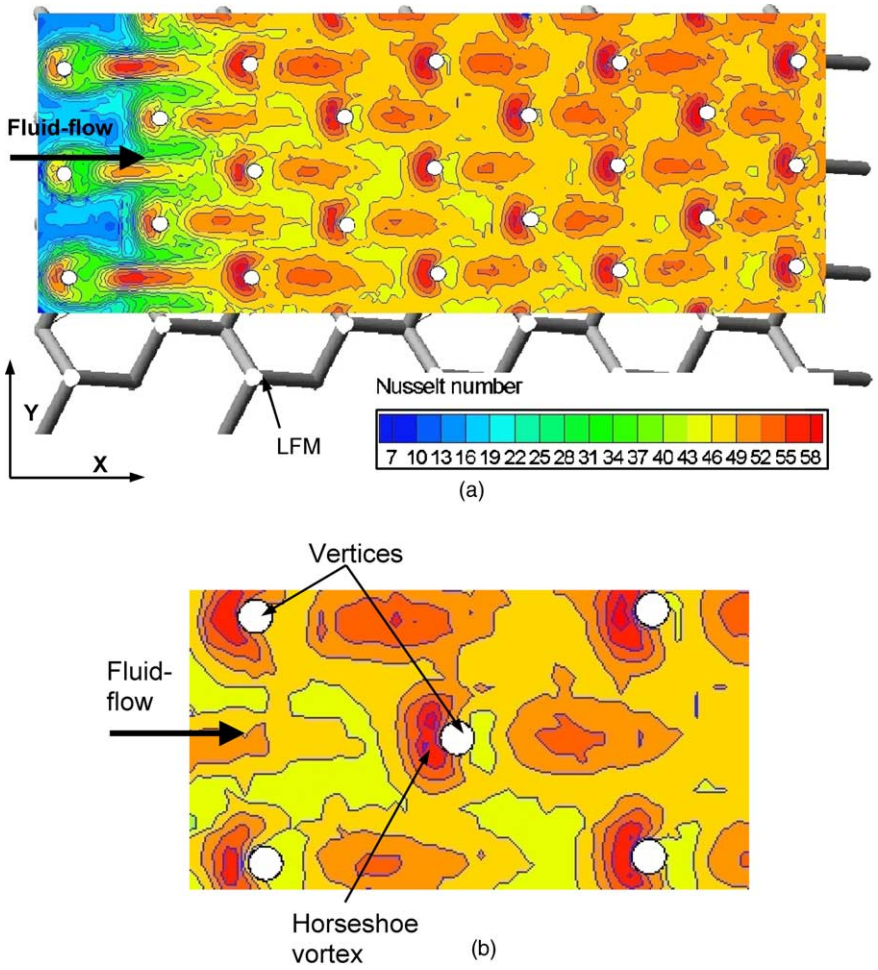

Fig. 6. (a) Distribution of local Nusselt number on endwall of O-A at $Re_{dp} = 4600$ and (b) enlarged view of two selected unit cells, showing the formation of horsevortex around each LFM vertex.

for both orientations is the same but each orientation has a different unit cell length, d_p. Therefore, they contain different number of unit cells along the flow direction: 8 for orientation A and 7 for orientation B.

The results of the present study reveal that exit region does not have any effect on the overall heat transfer along both orientations. It is believed that when there are many unit cells along the flow direction, the effects of the entry (and exit) become negligible compared to the overall endwall heat transfer.

4.4. Comparisons of the overall Nusselt numbers from steady-state and transient liquid crystal techniques

The TLC technique has been widely used as a way to obtain the local surface heat transfer distribution [10,11,14–17]. However, comparisons of the heat transfer data obtained from both the TLC and the conventional steady experiments are rarely made. This section compares the overall Nusselt numbers measured from all of the models with the polycarbonate LFM core. It should be noted that, for these models, it is assumed that there is no conduction along the struts and therefore no convection from their surfaces.

Fig. 9 presents the overall Nusselt numbers obtained from both the transient and the steady-state measurements. The three data points for orientation A from the TLC measurements were obtained after averaging over the endwall surface area. They show good agreement (to within ±16%) with the data obtained from the steady-state measurements with the aluminum endwall and polycarbonate core.

According to Coleman and Steele [12], the uncertainty in heat transfer coefficient h associated with both steady-state and transient measurements varies depending on the value of h. For instance, a smaller error from transient measurements than that from steady-state measurements is expected when $h < 100$ W/m^2 K. For

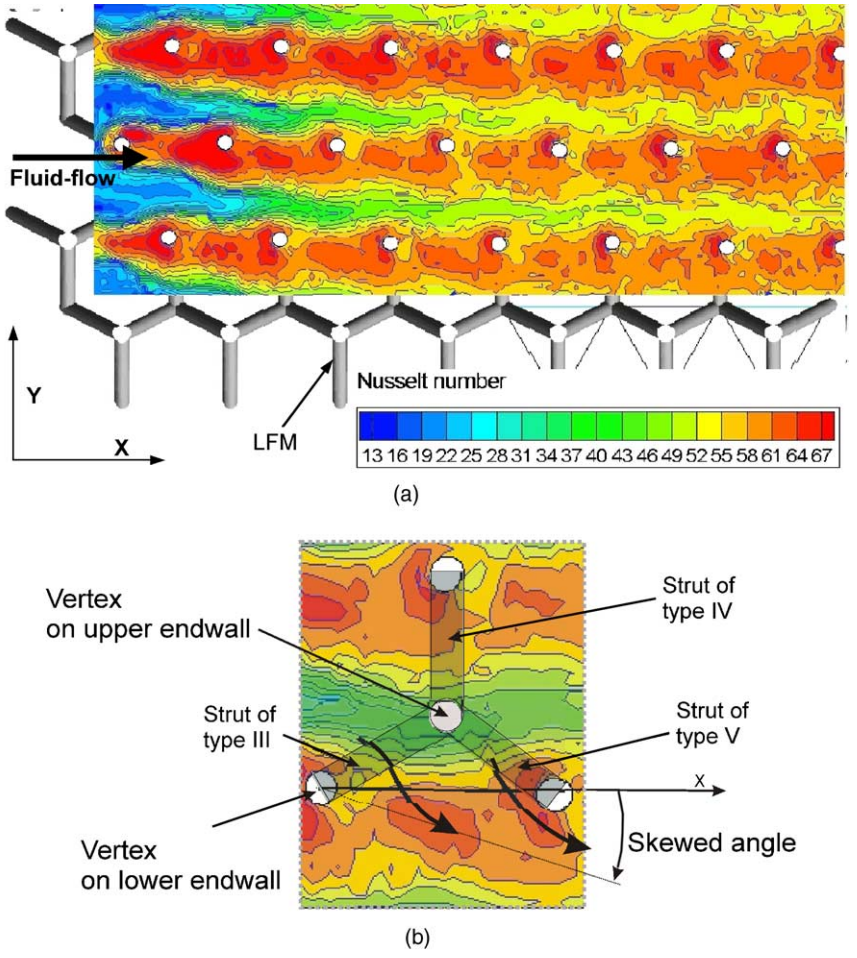

Fig. 7. (a) Distribution of local Nusselt number on endwall of O-B at $Re_{dp} = 6000$ and (b) enlarged view of a selected unit cell.

the higher heat transfer regime ($h > 150$ W/m^2 K), the opposite is expected. Therefore, in the transition regime ($100 < h < 150$ W/m^2 K), it is possible to achieve good agreement between both experiments. For the polycarbonate models tested in [9] and in the current study, the heat transfer coefficient falls within this range.

4.5. Effect of the orientation on the overall heat transfer performance

Fig. 9 presents the overall Nusselt number variation of the LM25 models of both orientation A and B. In previously reported steady-state forced convection experiments on the LFM with constant heat flux conditions [9], the overall heat transfer was characterized. The results are correlated as a function of Reynolds number as follows:

$$Nu_{dp} = C_1 (Re_{dp})^n \quad (6)$$

where the empirical constant C_1 and power index n are given in Table 3.

According to Fig. 9, both orientations of the LM25 models behave in a similar manner, having a very similar empirical constant (~1.0) and a power index (~0.55). Likewise, the polycarbonate models of orientation A and orientation B used in the TLC transient experiments also show a very similar heat transfer performance. These results imply that the rate of heat transfer from the struts and from the endwalls do not depend on the orientation of the LFM. These results are also surprising as orientation A has approximately twice the pressure loss of orientation B. This will be the subject of future work.

4.6. Effect of solid thermal conductivity of the LFM struts

The heat transfer in the test models is dominated by two mechanisms: (a) conduction and then convection

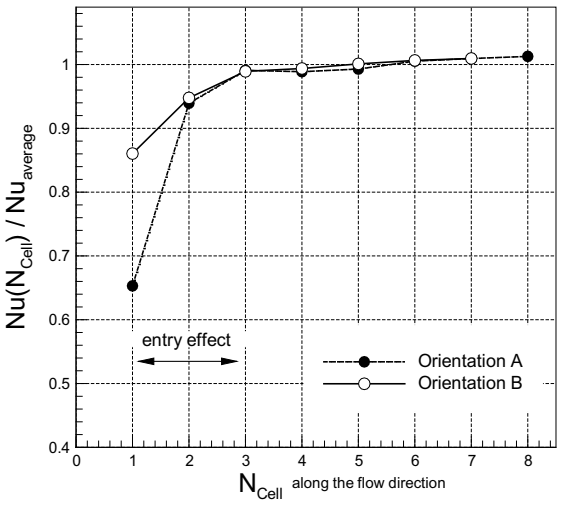

Fig. 8. Variations of the cell averaged Nusselt numbers along the flow direction for both orientations at $Re_{dp} = 4600$ for orientation A and $Re_{dp} = 6000$ for orientation B.

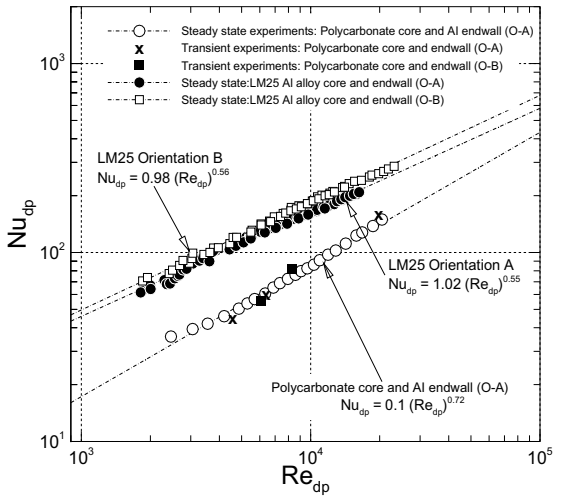

Fig. 9. Averaged Nusselts number obtained from both steady-state and transient measurements plotted as a function of Reynolds number for polycarbonate and aluminum alloy LFM samples.

Table 3
Constants for empirical correlations

Specimen	C_1	n
LM25 O-A	1.02	0.55
LM25 O-B	0.98	0.56
P O-A	0.1	0.72

from the solid struts, and (b) convection from the endwall surfaces. Because of the high porosity of the LFM structure, the percentage of the endwall area that is attached to the struts is small, less than 5%. This may prompt one to believe that mechanism (b) is dominant. If so, the overall surface heat transfer coefficient of the LFM heat exchanger with a high conductivity material such as LM25 would not be much larger than that with a low conducting material such as polycarbonate. According to Hunt and Tien [18], if the ligaments of high porosity materials are thin, conduction might not be significant. They concluded that the overall rate of heat transfer was independent of solid thermal conductivity in such high porosity materials. This section attempts to experimentally evaluate the effect of solid thermal conductivity on the overall heat transfer performance of the LFM model having a porosity of 0.94.

Steady-state experiments were carried out using two LFM models. The LM25 and polycarbonate models in orientation A were used to investigate the effect of solid thermal conductivity. The core structure of the latter model was made of polycarbonate and was sandwiched between 1 mm thick pure aluminum plates. Therefore, for this model, conduction through the LFM struts was expected to be negligible.

Fig. 9 shows the results of the overall Nusselt numbers of the LM25 models (both orientation A and B) and of the polycarbonate model (orientation A only) with the Al endwalls. In this section, only orientation A of the LM25 and polycarbonate models is considered. However, the results to be discussed here are likely to be applicable to orientation B. This is because the overall heat transfer shows almost no dependence on the orientation of the LFM, as mentioned in Section 4.5.

Fig. 10 shows the overall Nusselt number of the polycarbonate model Nu_{dp} (P), normalized by that of the

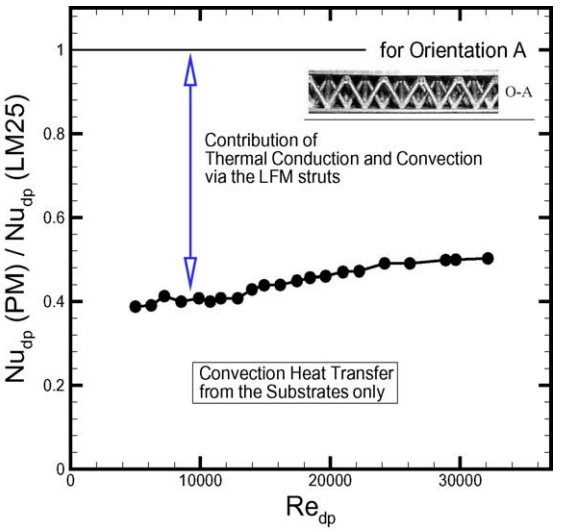

Fig. 10. Contribution of solid thermal conductivity in the overall heat transfer enhancement.

LM25 Al alloy model Nu_{dp} (LM25), as a function of Reynolds number. It is seen that approximately 2.5 times higher heat transfer enhancement can be achieved by simply replacing the polycarbonate LFM core with the aluminum alloy core. Consequently, LFM struts made of high thermal conductivity material can lead to significant heat transfer enhancement not only as a result of increased flow mixing but also due to convection from the strut surfaces via conduction to the LFM structure from the endwalls.

Fig. 9 showed that there is difference in slope of the Nu_{dp} versus Re_{dp} correlation between LM25 ($n = 0.55$) and polycarbonate ($n = 0.72$) models. This is due to the difference in the solid thermal conductivity of the core materials. In Fig. 10, this difference reveals itself as a reduction in the relative proportion of heat transfer that occurs from the struts as the Reynolds number rises.

5. Conclusions

The endwall heat transfer and fluid flow characteristics of highly porous, ultralightweight lattice-frame materials consisting of a 3D network of triangulated cylindrical struts were studied experimentally, with focus placed on the influence of the LFM morphology on the endwall flow and heat transfer patterns.

The pressure loss across a unit cell was found to be between 30% and 60% of the dynamic pressure for the range of Reynolds numbers considered. The pressure loss depends strongly on the orientation of the LFM due to its structural anisotropy. It was found, surprisingly, that both orientations of the LFM have almost the same heat transfer performance. Orientation B, which has the most open flow passage, had the lowest pressure losses.

Detailed endwall heat transfer distributions were obtained using the transient liquid crystal thermography. The formation of the vortical structures including the horseshoe vortices and the flow recirculation and reattachment around the LFM vertices increases the local endwall surface heat transfer, resulting in enhanced overall heat transfer. Spatially averaged Nusselt numbers from the transient experiments agree well with those obtained from steady-state measurements.

Although the LFM structure is highly porous, with a porosity of 0.94, it was found that over half of the heat is conducted from the heated endwall through the solid struts and then transferred to the fluid by convection from the surface of the struts, provided a high conductivity material is used.

Acknowledgements

This work was supported by the UK Engineering and Physical Sciences Research Council (EPSRC grant number EJA/U83) and the US Office of Naval Research (ONR grant number N000140110271). The authors wish to thank Dr. Peter Ireland of Osney Laboratory, Oxford University, for advices regarding the transient heat transfer experiments using thermochromic liquid crystals.

References

[1] A.-F. Bastawros, A.G. Evans, H.A. Stone, Evaluation of cellular metal heat dissipation media, Technical Report MECH 325, DEAS, Harvard University, 1998.
[2] T.J. Lu, Heat transfer efficiency of metal honeycombs, Int. J. Heat Mass Transfer 42 (1999) 2031–2040.
[3] T.J. Lu, H.A. Stone, M.F. Ashby, Heat transfer in open-cell metal foams, Acta Mater. 46 (10) (1998) 3619–3635.
[4] T.J. Lu, Ultralight porous metals: from fundamentals to applications, Acta Mech. Sin. 18 (5) (2002) 457–479.
[5] C.Y. Zhao, T. Kim, T.J. Lu, H.P. Hodson, Modeling on thermal transport in cellular metal foams, J. Thermofluid Phys. (in press) (also in: 8th Joint AIAA/ASME Thermophysics and Heat Transfer Conference, AIAA Paper # 2002-3014, St. Louis, USA, June 2002).
[6] C. Chen, T.J. Lu, N.A. Fleck, Effect of imperfections on the yielding of two-dimensional foams, J. Mech. Phys. Solids 47 (1999) 2235–2272.
[7] V.S. Deshpande, N.A. Fleck, M.F. Ashby, Effective properties of the octet-truss lattice material, J. Mech. Phys. Solids 49 (2001) 1747–1769.
[8] V.S. Deshpande, N.A. Fleck, Collapse of truss core sandwich beams in 3-point bending, Int. J. Solids Struct. 38 (2001) 6275–6305.
[9] T. Kim, C.Y. Zhao, H.P. Hodson, T.J. Lu, Convective heat dissipation with lattice-frame materials, Mech. Mater. (in press).
[10] D.R.H. Gillespie, Intricate internal cooling systems for gas turbine blading, D.Phil. Thesis, Department of Engineering Science, University of Oxford, UK, 1996.
[11] P.T. Ireland, A.J. Needly, D.R.H. Gillespie, A.J. Robertson, Turbulent heat transfer measurements using liquid crystals, Int. J. Heat Fluid Flow 20 (1999) 355–367.
[12] H.W. Coleman, W.G. Steele, Experimentation and uncertainty analysis for engineers, second ed., John Wiley and Sons, New York, 1999.
[13] T. Kim, A.J. Fuller, H.P. Hodson, T.J. Lu, An experimental study of thermal transport in lightweight metal foams at high Reynolds numbers, in: Proceedings of the International Symposium on Compact Heat Exchangers, Grenoble, France, August 2002, pp. 227–232.
[14] T. Kim, H.P. Hodson, T.J. Lu, Thermal flow behaviour around inclined single cylinders, Technical Report, Cambridge University Engineering Department, 2002.
[15] D.E. Metzger, R.A. Berry, J.P. Bronson, Developing heat transfer in rectangular duct with staggered pin fins, ASME Trans. J. Heat Transfer 104 (1982) 700–706.
[16] W.M. Yan, R.C. Hsieh, C.Y. Soong, Experimental study of surface-mounted obstacle effects on heat transfer enhancement by using transient liquid crystal thermograph, ASME Trans. J. Heat Transfer 124 (2002) 762–769.

[17] J.J. Hwang, C.-C. Lui, Measurement of endwall heat transfer and pressure drop in a pin-fin wedge duct, Int. J. Heat Mass Transfer 45 (2002) 877–889.

[18] M.L. Hunt, C.L. Tien, Effects of thermal dispersion on forced convection in fibrous media, Int. J. Heat Mass Transfer 31 (1988) 301–309.